Debonding and fracture of ceramic islands on polymer substrates

Jeong-Yun Sun, Nanshu Lu, Juil Yoon, Kyu-Hwan Oh, Zhigang Suo et al.

Citation: J. Appl. Phys. **111**, 013517 (2012); doi: 10.1063/1.3673805
View online: http://dx.doi.org/10.1063/1.3673805
View Table of Contents: http://jap.aip.org/resource/1/JAPIAU/v111/i1
Published by the American Institute of Physics.

Related Articles

The tensile strengths of heterogeneous interfaces: A comparison of static and dynamic first-principles calculations
J. Chem. Phys. 135, 244706 (2011)

Temperature-induced anomalous brittle-to-ductile transition of bulk metallic glasses
Appl. Phys. Lett. 99, 241907 (2011)

Size effects on the fatigue behavior of bulk metallic glasses
J. Appl. Phys. 110, 113507 (2011)

Mechanical response of nanometer thick self-assembled monolayers on metallic substrates using classical nanoindentation
J. Appl. Phys. 110, 114301 (2011)

How does spallation microdamage nucleate in bulk amorphous alloys under shock loading?
J. Appl. Phys. 110, 103519 (2011)

Additional information on J. Appl. Phys.

Journal Homepage: http://jap.aip.org/
Journal Information: http://jap.aip.org/about/about_the_journal
Top downloads: http://jap.aip.org/features/most_downloaded
Information for Authors: http://jap.aip.org/authors

ADVERTISEMENT

Downloaded 10 Jan 2012 to 146.6.102.180. Redistribution subject to AIP license or copyright; see http://jap.aip.org/about/rights_and_permissions

Debonding and fracture of ceramic islands on polymer substrates

Jeong-Yun Sun,[1,2] Nanshu Lu,[2] Juil Yoon,[3] Kyu-Hwan Oh,[1] Zhigang Suo,[2] and Joost J. Vlassak[2,a)]
[1]*Department of Material Science and Engineering, Seoul National University, Seoul 151-742, South Korea*
[2]*School of Engineering and Applied Sciences, Harvard University, Cambridge, Massachusetts 02138, USA*
[3]*Department of Mechanical Systems Engineering, Hansung University, Seoul 136-792, South Korea*

(Received 29 September 2011; accepted 6 December 2011; published online 10 January 2012)

We perform *in-situ* uniaxial tensile tests on polyimide substrates with patterned ceramic islands. The islands fail by either channel cracking or debonding from the substrate, depending on island size and thickness. To understand why different failure modes occur, we have analyzed the fracture and debonding of stiff islands on deformable substrates. Using finite element simulations, we find that the maximum tensile strain in the islands increases with island size, but decreases with island thickness. The maximum energy release rate for island/substrate debonding, in contrast, increases with both island size and thickness. Assuming that the islands do not fracture if the maximum tensile strain in the islands is lower than a critical value and that no debonding occurs if the maximum energy release rate is smaller than the interfacial toughness, the critical substrate strains for island fracture and debonding can be calculated. If the islands are thick and small, the critical debonding strain is small, and the islands fail by debonding. If the islands are large and thin, the critical fracture strain is small, and the islands fail by channel cracking. When the two critical strains are similar, debonding and cracking are expected to co-exist. Experimental observations confirm these findings. © *2012 American Institute of Physics*. [doi:10.1063/1.3673805]

I. INTRODUCTION

Flexible electronic devices are key components of a number of important technologies.[1–6] These devices often integrate a deformable polymer substrate to support inorganic functional materials, including semiconductors, metals, and ceramics. Although the polymer substrate can undergo large deformation, the inorganic materials usually fracture at strains below 1%.[7] One approach to reduce the strain in the inorganic components is to fabricate them into isolated islands on top of the polymer substrate.[7–11] Stretchability as large as 25% has been demonstrated using particle desorption mass spectrometry (PDMS)-supported SiN_x islands.[7,11] Several failure modes are observed for these polymer-bonded ceramic islands. For example, SiN_x islands on polyimide (PI) substrates have been reported to either crack[12] or debond[10] when subjected to uniaxial tension. Therefore, a reliability analysis of an array of islands supported by a polymer substrate must involve a consideration of both failure modes. Given proper failure criteria, there exists a critical failure strain for each failure mode and the smaller of these strains represents the critical strain for the structure. If the strain applied to the substrate exceeds this limit, the failure mode with the smaller critical failure strain occurs.

Cracking and debonding of substrate-bonded thin films have been studied systematically. Channel cracks in thin films bonded to a rigid substrate approach a steady state at crack lengths on the order of the film thickness.[13] However, when the substrate is much more compliant than the film, a steady state cannot be reached until the crack length exceeds multiple times the film thickness.[17] Moreover, the steady-state energy release rate increases significantly as the film-to-substrate stiffness ratio becomes large.[14] Since the sizes of preexisting flaws in a film are often on the order of the film thickness, the steady-state energy release rate can be used as the driving force for the initiation of channel cracks in films on stiff substrates, but not on compliant substrates.

For film/substrate interface debonding, Hutchinson and Suo[15] provided an analytical formula for the steady-state energy release rate as a function of the film-to-substrate stiffness and thickness ratios. He *et al.*[16] derived an analytical solution for the so-called convergent debonding case, where the length of the bonded interface is much smaller than the film thickness. Yu *et al.*[18] first investigated the effect of an interior edge on the delamination behavior of a patterned film. Lu *et al.*[19] modeled periodic stiff islands on a compliant substrate and showed that the energy release rate peaks at a debonding length much smaller than the film thickness and that it drops off immediately thereafter because of the large elastic mismatch and the finite size of the islands. The peak energy release rate can thus be used as a conservative criterion for island/substrate debonding.

The goal of this paper is to combine the analysis of cracking and debonding of stiff islands patterned on soft substrates to provide an explanation for the different failure modes observed experimentally. For a given island configuration, one can predict the critical substrate strain below which the islands are safe from either cracking or debonding. Equivalently, if the substrate strain is prescribed, the critical island geometry can be determined.

The plan of this paper is as follows. In Sec. II, we elucidate the experimental details of the fabrication of SiN_x island

a)Electronic mail: vlassak@seas.harvard.edu.

 © 2012 American Institute of Physics

Downloaded 10 Jan 2012 to 146.6.102.180. Redistribution subject to AIP license or copyright; see http://jap.aip.org/about/rights_and_permissions

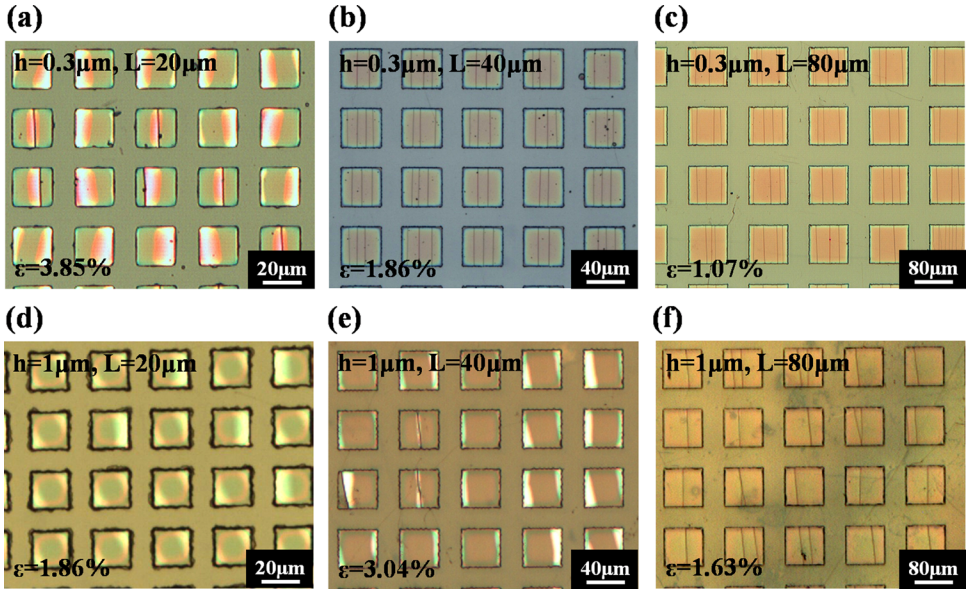

FIG. 1. (Color online) SiN_x islands on PI substrate stretched horizontally. Island thickness h and island size L are shown at the upper left corner of each micrograph. The substrate elongation ε_{appl} is given at the lower left corner. For islands with $h = 0.3$ μm (a)–(c), debonding and cracking coexist when $L = 20$ μm. When $L > 20$ μm, only channel cracking occurs. For islands with $h = 1$ μm (d)–(f), debonding and cracking coexist when $L = 40$ μm. When $L < 40$ μm, only debonding occurs; when $L > 40$ μm, only cracking takes place.

arrays on PI substrates and the *in-situ* uniaxial tensile tests. Experimental results are given in Sec. III, including the various failure modes for different island configurations and the corresponding failure strains. In Sec. IV, we describe the finite element simulations used to calculate the driving forces for island cracking and debonding, and we compare the simulation results with our experimental observations. Concluding remarks are given in Sec. V.

II. EXPERIMENTAL

Periodic SiN_x islands were fabricated on 25 μm thick PI substrates (Upilex-S, UBE Industries) using the following lift-off procedure: The PI substrates were ultrasonically cleaned using methanol and acetone and attached to a 3 mm thick aluminum (Al) plate using double-sided tape. The PI/Al assemblies were kept in a vacuum chamber for 24 h to eliminate any air bubbles. A 3.2-μm-thick positive photoresist (S1818, Microposit) was then spin-coated on top of the PI substrates. The coated substrates were baked for 2 min at 115 °C and exposed for 3 s to light intensities of 28.9 mW/cm^2 (I-line) and 59.1 mW/cm^2 (G-line) through a chromium reticule using an MJB4 mask aligner (SUSS MicroTec). The samples were developed in a MF-319 photoresist developer (Microposit), rinsed in DI water for 1 min, and dried with N_2 gas. The PI substrates were then cut into 7 mm × 60 mm rectangular strips while still attached to the Al plates. Next, SiN_x films were deposited by chemical vapor deposition (CVD) in a NEXX system with a base pressure of 5×10^{-6} Torr. The depositions were performed at a working pressure of 10 mTorr with a flow of 40 sccm Ar—3% SiH_4, 5.8 sccm N_2, and 20 sccm Ar. The microwave power was 265 W, and the substrate temperature was kept at 22 °C. Finally, the SiN_x coatings were patterned by stripping the photoresist along with the extra SiN_x in acetone. Square islands of width L ranging from 10 μm to 120 μm and thickness h ranging from 100 nm to 1 μm were prepared. The island spacing S normalized by the island width, $S/L = 1.5$, was held constant for all specimens.

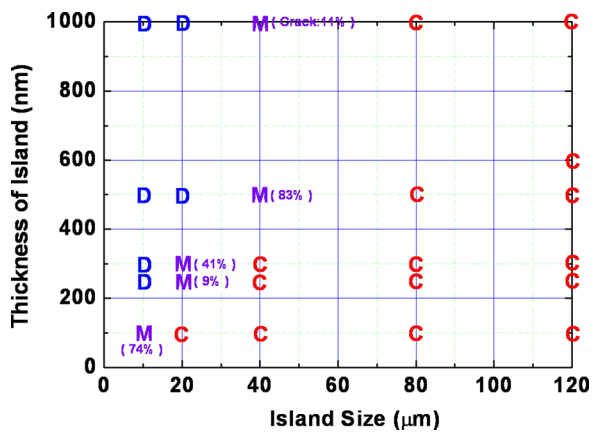

FIG. 2. (Color online) Summary of the failure modes for different island configurations. C—only cracking occurs. D—only debonding takes place. M—debonding and cracking coexist (the numbers indicate the proportion of cracked islands).

After detaching the samples from the Al plate, they were uniaxially stretched in a homemade screw-driven tensile device. A 5 mm × 5 mm square lattice of islands was placed half way between the two grips to achieve a uniform tensile state. All tensile tests were performed *in-situ* under an optical microscope with a CCD camera. Applied strains were measured directly on the recorded micrographs.

III. EXPERIMENTAL RESULTS

Figure 1 shows typical micrographs of the deformed islands. All samples were stretched in the horizontal direction. Different failure modes can be identified for different island configurations. Figures 1(a) to 1(c) show islands of the same thickness, $h = 0.3$ μm, but of different size: $L = 20$ μm, 40 μm, and 80 μm, respectively. Large islands fail by channel cracking, as shown in Figs. 1(b) and 1(c). Parallel channel cracks run across the islands in the direction perpendicular to the applied load. When the island size decreases to 20 μm, however, some islands also debond as indicated by the brightened areas in Fig. 1(a). A similar situation is

Downloaded 10 Jan 2012 to 146.6.102.180. Redistribution subject to AIP license or copyright; see http://jap.aip.org/about/rights_and_permissions

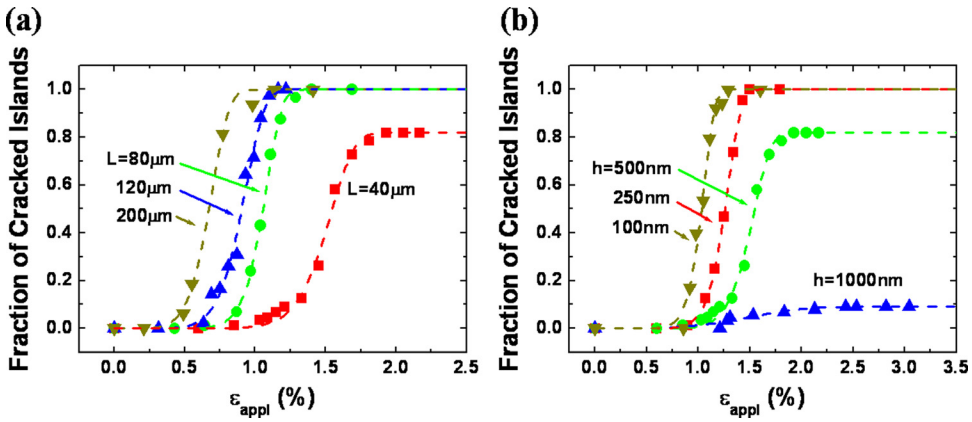

FIG. 3. (Color online) The accumulated fraction of cracked islands is plotted as a function of the applied strain. The experimental observations are plotted as dots and the Weibull distributions are plotted as dashed lines. (a) Island size is varied with fixed island thickness ($h = 500$ nm). (b) Island thickness is varied with fixed island size ($L = 40$ μm). If cracking and debonding coexist, the curve cannot reach unity because debonded islands do not crack.

observed for 1-μm-thick islands (Figs. 1(d)–1(f)). Islands with a size of 80 μm fail by channel cracking (Fig. 1(f)), whereas 40-μm-large islands can either fracture or debond (Fig. 1(e)). When islands become even smaller, i.e., $L = 20$ μm, only debonding is observed (Fig. 1(d)). When comparing micrographs in each column, it is evident that thicker islands are more prone to debonding for a given island size. In Figs. 1(a) and 1(e), individual islands either fracture or debond from the edges of the islands, although in some cases fracture is followed by debonding from the fractured edge. The reverse is never observed. All channel cracks run immediately across the entire island, i.e., fracture is an almost instantaneous process. By contrast, it is possible to observe partial interfacial cracks indicating that interfacial debonding is a quasi-static process. As the applied strain increases and debonding progresses, the energy release rate is reduced and eventually approaches zero. Consequently, fully debonded islands were not observed in our experiments.

The failure modes for all island configurations are summarized in Fig. 2. The horizontal axis represents island size and the vertical axis the island thickness. We create a failure mode map by designating the experimentally observed failure modes as follows: C indicates that all islands showed channel cracking for a given combination of island size and thickness; D is used when only island debonding is observed, while M denotes a mixed failure mode where some islands debond and others fracture. It is clear from the figure that for a given island thickness, the failure mode changes from debonding to channel cracking as island size increases. For a given island size, the failure mode changes from cracking to debonding as the island thickness increases.

Island dimensions also affect the failure strain. Figure 3 plots the accumulated fraction of fractured islands as a function of the strain applied to the substrate. From 50 to 88 islands are explored for each case, and the accumulated fraction of fractured islands are fitted using Weibull distribution,

$$F(x) = A\left(1 - e^{-(x/\lambda)^{\kappa}}\right), \tag{1}$$

where A, κ, and λ are fitting parameters. In the context of this paper, we define the fracture strain, ε_f, as the substrate strain at which 1% of the islands are fractured, i.e., $F(\varepsilon_f)/A = 0.01$. For islands with a fixed thickness of 500 nm, the fracture strain increases as the island size decreases, as shown in Fig. 3(a). For islands with a fixed size of 40 μm, the fracture strain increases as the island thickness increases, as shown in Fig. 3(b). Some of the curves do not reach 100%, indicating that not all islands fracture: Indeed some islands debond first. The strain in these islands is released and channel cracks cannot form. Similar cumulative distribution functions are shown in Fig. 4 with an emphasis on debonding. The accumulated fraction of debonded islands is plotted as a function of the applied strain for different sizes (Fig. 4(a)) and different thicknesses (Fig. 4(b)), along with the Weibull fit. Similar to the fracture case, the debonding strain, ε_d, is defined as the substrate strain at which 1% of the islands are debonded. When the island thickness is fixed at 250 nm, the debonding strain increases with decreasing

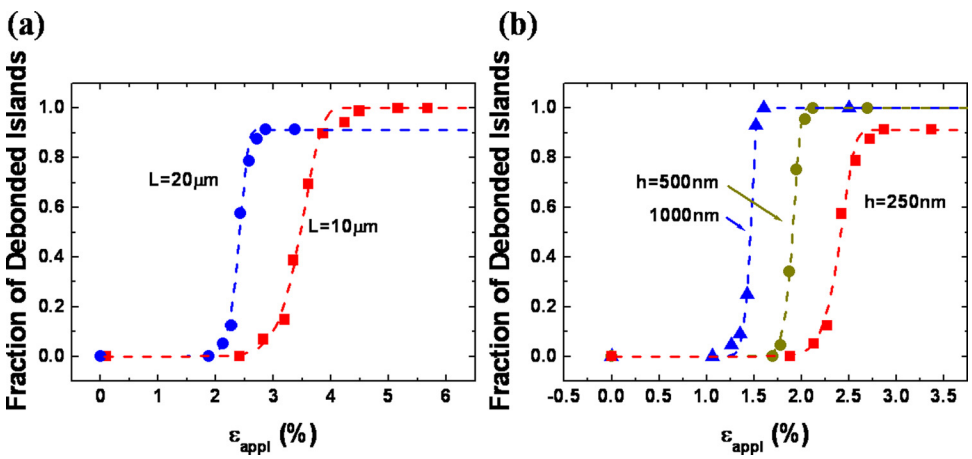

FIG. 4. (Color online) The accumulated fraction of debonded islands is plotted as a function of the applied strain. The experimental observations are plotted as dots and the Weibull distributions are plotted as dashed lines. (a) $h = 250$ nm is fixed, island size is varied. (b) $L = 20$ μm is fixed, island thickness is varied. If cracking and debonding coexist, the curve cannot reach unity because cracked islands do not debond from the edge of the island.

Downloaded 10 Jan 2012 to 146.6.102.180. Redistribution subject to AIP license or copyright; see http://jap.aip.org/about/rights_and_permissions

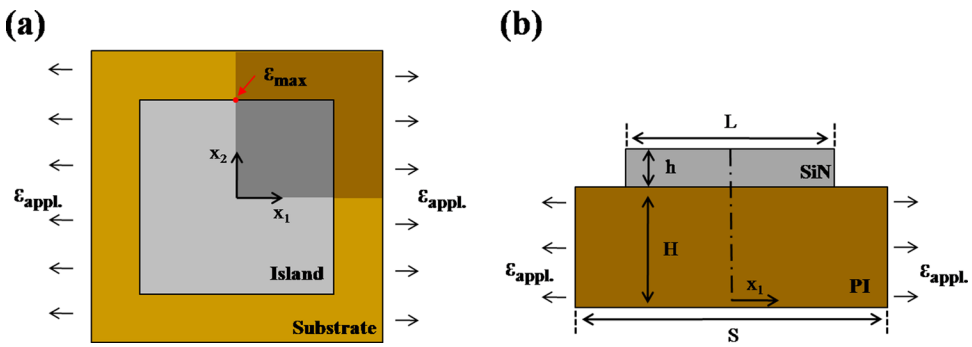

FIG. 5. (Color online) Schematics of the 3D finite element model of a unit cell: (a) top view and (b) side view. $S/L = 1.5$ is fixed in all the experiments and simulations. Due to the symmetry, only the shaded quarter in (a) is modeled. The maximum tensile strain is found at the root of the center of the edge, as marked by ε_{max}.

island size, as shown in Fig. 4(a). For a given island size of 20 μm, the debonding strain increases with decreasing island thickness. We will analyze these trends using mechanics in Sec. IV A.

IV. SIMULATION AND ANALYSIS

A. Fracture analysis

Using the commercial finite element code ABAQUS 6.7-1, we established a three-dimensional model of a unit cell of the periodic island lattice. Schematics of the top and side views of the model are shown in Fig. 5. Because of the four-fold symmetry, only one quarter of the unit cell was modeled, as represented by the shaded area in Fig. 5(a). We modeled the islands and the substrate as homogeneous, isotropic linear elastic materials with Young's moduli $E_{SiN} = 200$ GPa and $E_{PI} = 9.2$ GPa, and with Poisson's ratios $\nu = 0.3$ for both SiN_x and PI. The lattice periodicity was fixed at $S/L = 1.5$ for all simulations. A uniform displacement u_{appl} was applied to the substrate in the x_1-direction, corresponding to a strain of $\varepsilon_{appl} = 2u_{appl}/S$. We used 3D brick elements to mesh both the island and the substrate. Ten elements were assigned across the island thickness. A refined mesh was used to confirm that there was no mesh dependence of the strain field across the island thickness.

The maximum tensile strain in the island, ε_{max}, occurs at the root of the center of the island edge, as labeled in Fig. 5(a). Figure 6(a) plots the maximum strain normalized by the applied substrate strain as a function of island size for various island thicknesses. It demonstrates that smaller islands experience smaller strains for a given island thickness. For a given island size, thicker islands experience somewhat smaller strains. A simple one-dimensional model to estimate the strain in the islands is considered. Under an applied strain ε_{appl}, the strain in the island and the segment of the substrate covered by the island is ε_1, while the strain in the segments of bare substrate is ε_2. Considering that each segment of the structure carries the same force, it follows that

$$E_f h\varepsilon_1 + E_s H\varepsilon_1 = E_s H\varepsilon_2. \tag{2}$$

The total elongation of the structure under ε_{appl} consists of two parts

$$\varepsilon_{appl} S = \varepsilon_1 L + \varepsilon_2 (S - L). \tag{3}$$

A combination of Eqs. (2) and (3) gives the strain in the island, ε_1

$$\frac{\varepsilon_1}{\varepsilon_{appl}} = \frac{1}{1 + \left(1 - \frac{L}{S}\right)\frac{E_f}{E_s}\frac{h}{H}}. \tag{4}$$

This one-dimensional model is in good qualitative agreement with the trends observed in Figs. 3(a) and 3(b).

To provide a more quantitative relationship between the experimental fracture strain and the calculated maximum strain, we adopt a simple failure criterion. The criterion is based on the assumption that an islands fractures when the maximum strain in the islands reaches a critical value, $\varepsilon_{max} = \varepsilon_c$, or equivalently that the size distribution of pre-existing flaws in the islands is independent of island size or thickness. The experiments and calculations are then related through

$$\frac{\varepsilon_c}{\varepsilon_f} = \frac{\varepsilon_{max}}{\varepsilon_{appl}} = m\left(\frac{L}{h}, \frac{H}{h}\right), \tag{5}$$

where m is a strain concentration factor that depends on geometry and H denotes the substrate thickness. Equation (5) can

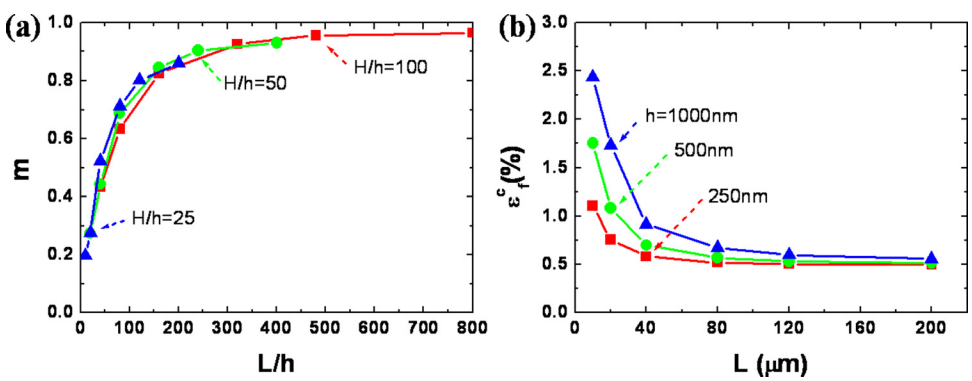

FIG. 6. (Color online) (a) FEM results of normalized maximum strains in the island and (b) critical strain-to-rupture calculated by Eq. (4), as functions of island size with various island thicknesses.

Downloaded 10 Jan 2012 to 146.6.102.180. Redistribution subject to AIP license or copyright; see http://jap.aip.org/about/rights_and_permissions

TABLE I. Critical local rupture strain, ε_c, calculated from Eq. (4) using the measured strain-to-fracture, ε_f, and Fig. 6(a) for various island configurations.

h (nm)	L (μm)	ε_c (%)
100	20	0.57
100	40	0.80
250	40	0.65
250	80	0.50
250	120	0.49
500	40	0.78
500	80	0.62
500	120	0.48
1000	80	0.58
1000	120	0.55

be used to determine ε_c from the experimental fracture strain, ε_f, and the simulation results for m shown in Fig. 6(a). Table I lists the critical strain ε_c calculated from Eq. (5) using the measured fracture strain. Evidently, there is some variation in the values of ε_c due to the statistical nature of preexisting flaws. If we take the critical island strain equal to the smallest experimental value, $\varepsilon_c = 0.48\%$, we obtain a conservative failure criterion for the SiN_x islands in this study. With this value for ε_c, Eq. (5) can be used to predict the critical substrate strain ε_f^c for any island. Figure 6(b) plots ε_f^c as a function of island size and island thickness using the values of m provided in Fig. 6(a). More than 99% of the islands of given size and thickness will be safe from fracture as long as the strain applied to the substrate is smaller than ε_f^c.

B. Debonding analysis

We now develop a criterion for island debonding. Debonding of a periodic array of stiff islands on polymer substrates has been analyzed by Lu *et al.*[19] They performed plane-strain finite element simulations of islands with interfacial cracks emanating from both edges of the islands. The energy release rate was found to peak at a crack length on the order of $0.1h$ and to drop rapidly as the cracks propagate. Evidently, if the maximum energy release rate is smaller than the interfacial toughness island/substrate debonding cannot occur. We adopt this approach to analyze the debonding observed in our experiments. Dimensional considerations dictate that the energy release rate should take the following form:

TABLE II. Interfacial toughness Γ_i, calculated from Eq. (7) using the measured strain-to-debond, ε_d, and Fig. 7(a) for various island configurations.

h (nm)	L (μm)	Γ_i (J/m^2)
250	10	11.3
250	20	9.4
500	20	9.6
1000	20	7.3
1000	40	6.0

$$G = \frac{E_f^* \varepsilon_{appl}^2 h}{2} f\left(\frac{a}{h}, \frac{L}{h}, \frac{H}{h}\right), \tag{6}$$

where a represents crack length, $E_f^* = E/(1 - V_f^2)$, and f represents a dimensionless function that can be determined from finite element simulations. The calculated energy release rate for a given island configuration reaches a maximum at a very small value of a/h and decreases almost linearly immediately thereafter (not shown). Consequently, interfacial cracks arrest when the energy release rate drops below the interfacial toughness resulting in partially debonded islands as shown in Figs. 1(a), 1(d), and 1(e). Unlike channel cracks, which propagate quickly across an island, debonding cracks grow in a stable fashion with increasing substrate deformation. The maximum energy release rate G_{max} can be written as a function of L/h and H/h,

$$G_{max} = \frac{E_f^* \varepsilon_{appl}^2 h}{2} g\left(\frac{L}{h}, \frac{H}{h}\right), \tag{7}$$

where g is a dimensionless function plotted in Fig. 7(a) for various values of L/h and H/h. It is evident from the figure that, if the film is much thinner than the substrate, g is a function of L/h only. In that case, g increases with increasing island size and decreasing island thickness.

Taking $G_{max} = \Gamma_i$ as the criterion for island debonding, where Γ_i denotes the interfacial toughness, we find from Eq. (7)

$$\varepsilon_d^c = \sqrt{\frac{2\Gamma_i}{E_f^* h g}}, \tag{8}$$

where ε_d^c is the substrate strain at which debonding occurs. Similar to Sec. IV A, we use the experimental values of ε_d^c to

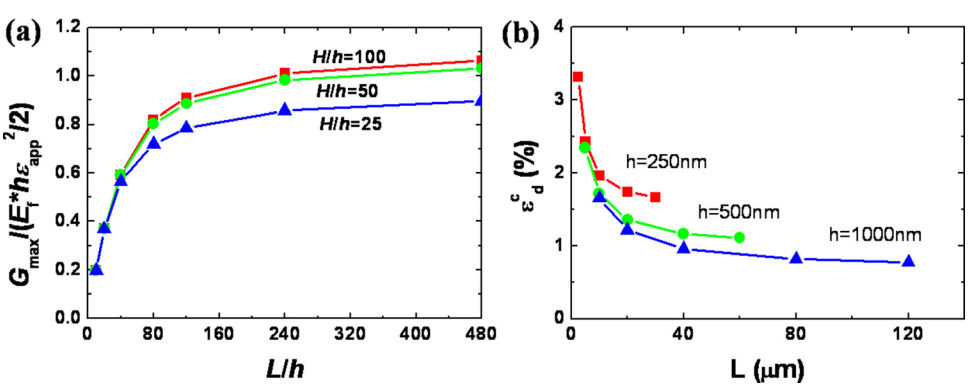

FIG. 7. (Color online) (a) FEM results of the normalized maximum energy release rate and (b) critical applied strain-to-debond calculated by Eq. (7), as a function of island size for various island thicknesses.

Downloaded 10 Jan 2012 to 146.6.102.180. Redistribution subject to AIP license or copyright; see http://jap.aip.org/about/rights_and_permissions

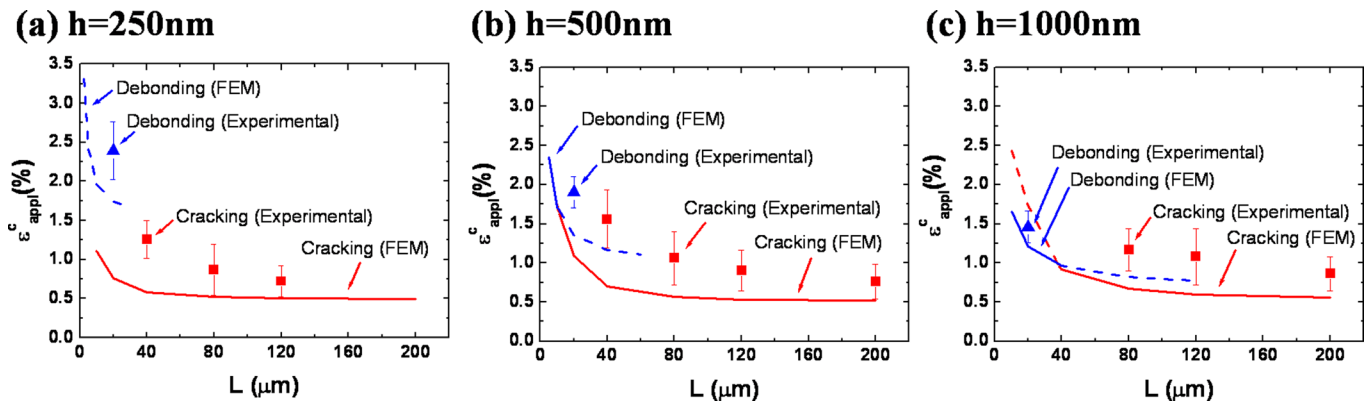

FIG. 8. (Color online) Combining Figs. 6(b) and 7(b), the critical applied strains to debond or to rupture are plotted as functions of island size for various island thicknesses: (a) $h = 250$ nm, (b) $h = 500$ nm, and (c) $h = 1000$ nm. The measured strain-to-rupture and strain-to-debond are plotted as square and triangular symbols, respectively, to compare with the theoretical prediction. For a given island configuration, the failure mode with the lower critical applied strain is predicted to occur.

calculate Γ_i and then take this Γ_i as an interfacial property to predict the critical debonding for different island geometries. Table II lists the Γ_i obtained using different island configurations. There is some variation in the values of Γ_i due to the statistical nature of preexisting flaws. Using the smallest interfacial toughness value $\Gamma_i = 6.0J/m^2$ in Eq. (8), we obtain a conservative criterion for delamination of the islands. The results are depicted in Fig. 7(b). As expected, the critical debonding strain decreases with increasing island size or thickness. An applied strain smaller than the critical value will cause fewer than 1% of the islands to debond. Alternately, if a maximum substrate deformation is specified, we can use the criterion to predict the island size or thickness, below which no debonding will occur.

C. Determination of the critical loading and the failure mode

By combining the results from Secs. IV A and IV B, it is now possible to predict which failure mechanism will occur for a given island geometry. Figure 8 shows the combined results from Figs. 6(b) and 7(b), i.e., the critical substrate strains for debonding and fracture. If the applied strain is lower than either strain for a given island configuration, neither island debonding nor fracture will occur. If the substrate strain is increased, the islands will eventually crack or delaminate depending on which critical strain is smaller. Taking islands with $h = 500$ nm and $L = 40$ μm for example, Fig. 8(b) provides a critical fracture strain of 1.05% and a critical debonding strain of 1.40%. Evidently these islands will fail by channel cracking instead of delamination.

The effects of island geometry on failure mode can be understood by examining the three pairs of curves shown in Fig. 8, which share very similar features. When islands are small, the critical debonding strain is lower than the critical fracture strain. Therefore, at small island size, debonding is the predicted failure mechanism and it is the only failure mode observed, as confirmed by Fig. 1(d). When islands are of some intermediate size, the values of the two critical strains are similar. In this case, both channel cracking and debonding of islands is observed within the same array of islands, as shown in Figs. 1(a) and 1(e). When the islands are larger still, the critical fracture strain drops below the critical debonding strain and all islands fail by channel cracking, as observed in Figs. 1(b), 1(c), and 1(f).

The experimental fracture and debonding strains are plotted as dots in Fig. 8. Since we used conservative failure criteria to predict the critical strains, the calculated critical strains can be regarded as lower bounds to the experimental failure strains as defined in this paper. The integrity of the islands can be guaranteed if the applied substrate strain is kept below the critical strains. In summary, Fig. 8 can be used in prediction of failure or design of islands, depending on the need. For a given island structure, the critical fracture and debonding strains are given by Fig. 8. To keep the islands intact, the applied strain cannot exceed either of the critical failure strains.

V. CONCLUSIONS

When subject to uniaxial stretching, ceramic islands on polyimide substrates exhibit different failure modes: smaller and thicker islands tend to fail by debonding, whereas larger and thinner islands are more prone to channel cracking. For intermediate island geometries, both channel cracking and debonding are observed. By assuming simple fracture and debonding criteria and by combining these with finite element simulations to calculate the driving forces for island fracture and debonding, we have obtained the critical substrate strains for channel cracking and debonding. These critical strains are in good agreement with our experimental observations.

ACKNOWLEDGMENTS

This work is supported by the National Science Foundation (NSF) under Grant CMS-0556169, and by the Materials Research Science and Engineering Center (MRSEC) at Harvard University. It was performed in part at the Center for Nanoscale Systems (CNS), a member of the National Nanotechnology Infrastructure Network (NNIN), which is

Downloaded 10 Jan 2012 to 146.6.102.180. Redistribution subject to AIP license or copyright; see http://jap.aip.org/about/rights_and_permissions

supported by the National Science Foundation under NSF Award No. ECS-0335765. CNS is part of the Faculty of Arts and Sciences at Harvard University. KHO is grateful for the support from the Information Technology Research Center (ITRC) granted by the Korea government (2011-0001460). JY is grateful for support from the National Research Foundation of Korea (KRF-2011-0003476).

[1]J. A. Rogers, Z. Bao, K. Baldwin, A. Dodabalapur, B. Crone, V. R. Raju, V. Kuck, H. Katz, K. Amundson, J. Ewing, and P. Drzaic, Proc. Natl. Acad. Sci. U.S.A. **98**, 4835 (2001).
[2]E. Bonderover and S. Wagner, IEEE Electron Device Lett. **25**, 295 (2004).
[3]C. J. Brabec, Sol. Energy Mater. Sol. Cells **83**, 273 (2004).
[4]E. Abad, S. Zampolli, S. Marco, A. Scorzoni, B. Mazzolai, A. Juarros, D. Gómez, I. Elmi, G. C. Cardinali, J. M. Gómez, F. Palacio, M. Cicioni, A. Mondini, T. Becker, and I. Sayhan, Sens. Actuator B **127**, 2 (2007).
[5]T. Someya, Y. Kato, T. Sekitani, S. Iba, Y. Noguchi, Y. Murase, H. Kawaguchi, and T. Sakurai, Proc. Natl. Acad. Sci. U.S.A. **102**, 12321 (2005).
[6]H. C. Ko, M. P. Stoykovich, J. Song, V. Malyarchuk, W. M. Choi, C.-J. Yu, J. B. Geddes III, J. Xiao, S. Wang, Y. Huang, and J. A. Rogers, Nature **454**, 748 (2008).
[7]S. P. Lacour, S. Wagner, R. J. Narayan, T. Li, and Z. Suo, J. Appl. Phys. **100**, 014913 (2006).
[8]P. I. Hsu, M. Huang, Z. Xi, S. Wagner, Z. Suo, and J. C. Stum, J. Appl. Phys. **95**, 705 (2004).
[9]S. Wagner, S. P. Lacour, J. Jones, P. I. Hsu, J. C. Sturm, T. Li, and Z. Suo, Physica E **25**, 326 (2005).
[10]R. Bhattacharya, A. Salomon, and S. Wagner, J. Electrochem. Society **153**, G259 (2006).
[11]J.-Y. Sun, N. Lu, J. Yoon, K.-H. Oh, Z. Suo, and J. J. Vlassack, J. Mater. Res. **24**, 3338 (2009).
[12]H. Gleskova, S. Wagner, and Z. Suo, Appl. Phys. Lett. **75**, 3011 (1999).
[13]T. Nakamura and S. Kamath, Mech. Mater. **13**, 67 (1992).
[14]J. L. Beuth, Int. J. Solids Struct. **29**, 1657 (1992).
[15]J. W. Hutchinson and Z. Suo, Adv. Appl. Mech. **29**, 63 (1992).
[16]M. Y. He, A. G. Evans, and J. W. Hutchinson, Acta Mater. **45**, 3481 (1997).
[17]R. Huang, J. H. Prevost, Z. Y. Huang, and Z. Suo, Eng. Fract. Mech. **70**, 2513 (2003).
[18]H. H. Yu, M. Y. He, and J. W. Hutchinson, Acta Mater. **49**, 93 (2001).
[19]N. Lu, J. Yoon, and Z. Suo, Int. J. Mater. Res. **98**, 717 (2007).

Downloaded 10 Jan 2012 to 146.6.102.180. Redistribution subject to AIP license or copyright; see http://jap.aip.org/about/rights_and_permissions